

# Dynamic control of 2D non-Hermitian photonic corner skin modes in synthetic dimensions

Received: 8 March 2024

Accepted: 4 December 2024

Published online: 30 December 2024


 Check for updatesXinyuan Zheng<sup>1,5</sup>, Mahmoud Jalali Mehrabad <sup>2,5</sup> , Jonathan Vannucci <sup>2</sup>, Kevin Li<sup>2</sup>, Avik Dutt <sup>3</sup>, Mohammad Hafezi <sup>2</sup>, Sunil Mittal <sup>4</sup>  & Edo Waks<sup>1</sup> 

Non-Hermitian models describe the physics of ubiquitous open systems with gain and loss. One intriguing aspect of non-Hermitian models is their inherent topology that can produce intriguing boundary phenomena like resilient higher-order topological insulators (HOTIs) and non-Hermitian skin effects (NHSE). Recently, time-multiplexed lattices in synthetic dimensions have emerged as a versatile platform for the investigation of these effects free of geometric restrictions. Despite holding broad applications, studies of these effects have been limited to static cases so far, and full dynamical control over the non-Hermitian effects has remained elusive. Here, we demonstrate the emergence of topological non-Hermitian corner skin modes with remarkable temporal controllability and robustness in a two-dimensional photonic synthetic time lattice. Specifically, we showcase various dynamic control mechanisms for light confinement and flow, including spatial mode tapering, sequential non-Hermiticity on-off switching, dynamical corner skin mode relocation, and light steering. Moreover, we establish the corner skin mode's robustness in the presence of intensity modulation randomness and quantitatively determine its breakdown regime. Our findings extend non-Hermitian and topological photonic effects into higher synthetic dimensions, offering remarkable flexibility and real-time control possibilities. This opens avenues for topological classification, quantum walk simulations of many-body dynamics, and robust Floquet engineering in synthetic landscapes.

Non-Hermitian systems host a range of intriguing phenomena in physics, such as reconfigurable light routing<sup>1</sup>, potential for enhanced sensitivity<sup>2,3</sup> and unidirectional invisibility<sup>4</sup>, that are deeply rooted in symmetry and topology. One such phenomenon is the non-Hermitian skin effect (NHSE) where a macroscopic fraction of the eigenmodes of a finite system become exponentially localized at its boundary<sup>5,6</sup>. This localization is a direct consequence of the nontrivial (topological) winding of the system's eigenvalues in the complex energy plane<sup>7-9</sup>.

Disorder and small variations in the system do not change the winding number which is a topological invariant<sup>9</sup>.

Over the last few years, the NHSE has been demonstrated on a variety of platforms<sup>5,10,11</sup>. Exemplary platforms include acoustics and phononics<sup>12</sup>, topo-electric circuits<sup>13</sup>, and photonics<sup>14</sup>. These developments are in part motivated by the profound impact of NHSE on band topology<sup>7,15,16</sup>, spectral symmetry<sup>17</sup>, and dynamics<sup>18,19</sup>. Particularly in photonics, recently the NHSE has enabled intriguing demonstrations

<sup>1</sup>Institute for Research in Electronics and Applied Physics, University of Maryland, College Park, MD, USA. <sup>2</sup>Joint Quantum Institute, University of Maryland, College Park, MD, USA. <sup>3</sup>Department of Mechanical Engineering, and Institute for Physical Science and Technology, University of Maryland, College Park, MD, USA. <sup>4</sup>Department of Electrical and Computer Engineering, Northeastern University, Boston, MA, USA. <sup>5</sup>These authors contributed equally: Xinyuan Zheng, Mahmoud Jalali Mehrabad.  e-mail: [mjalalim@umd.edu](mailto:mjalalim@umd.edu); [s.mittal@northeastern.edu](mailto:s.mittal@northeastern.edu); [edowaks@umd.edu](mailto:edowaks@umd.edu)

of the tuneable directional flow of light<sup>20</sup>, near-field beam steering<sup>21</sup>, engineering arbitrary band topology<sup>22</sup> and topological funneling of light<sup>14</sup>. Nevertheless, these demonstrations have been limited to systems that can be effectively described by time-independent Hamiltonians<sup>23</sup>. The introduction of time-dependent non-Hermitian Hamiltonians can lead to a dynamic control over the skin effect and also lead to fundamental advances in novel non-Hermitian topological phases that are not accessible using time-independent systems. Here we demonstrate dynamical control of the two-dimensional non-Hermitian photonic skin effect, that is, corner skin modes, using purely synthetic temporal dimensions. Specifically, using time-multiplexed light pulses in fiber loops, we show manipulation of the gain/loss in the system at a scale that is faster than the dynamics of light pulses in the lattice. Using this dynamical manipulation, we demonstrate gradual control over the degree of localization of the corner skin modes, gradual tweezing of light where we move the corner skin modes along a predefined trajectory in the lattice, and 2D funneling of light where photons always funnel to the corner skin modes irrespective of their initial position in the 2D lattice. Finally, by introducing controlled disorder in the system in the form of random variations in gain and loss, we quantitatively investigate the robustness of the corner skin modes against such disorders. Our work opens up an avenue to explore the rich physics of time-dependent non-Hermitian models such as non-Hermitian Floquet systems.

## 2d quantum walk with non-Hermitian topology

Our system simulates a discrete-time quantum walk of photons on a two-dimensional non-Hermitian square lattice, as illustrated schematically in Fig. 1a. Specifically, we implement a split-step walk where the walker first randomly steps to either left or right (corresponding to the  $X$  direction) with equal probability, then up or down (corresponding to the  $Y$  direction). To introduce non-Hermiticity, we introduce an additional gain  $e^{+\delta_x}$  when the walker steps to the left, and an additional loss  $e^{-\delta_x}$  when the walker steps to the right. Similarly, the walker experiences a gain  $e^{+\delta_y}$  when moving down and a loss of  $e^{-\delta_y}$  when moving up. The parameters  $\delta_x$  and  $\delta_y$  then indicate the degree of non-Hermiticity of the walk.

For this quantum walk, a concept of complex energy can analogously be defined, by solving for the eigenmodes of the non-unitary quantum walk evolution operator  $\hat{U}$  and taking the logarithm of the corresponding eigenvalue  $u_j$ . Namely, this can be formulated as  $\epsilon_j = i \log(u_j)$ , where  $\hat{U} |u_j\rangle = u_j |u_j\rangle$ . If we further impose periodic boundary conditions (PBCs) in both  $x$  and  $y$  for the bulk in Fig. 1a, we can apply the Bloch theorem for the walk and obtain the complex energy bands  $\epsilon_{up/down}(k_x, k_y)$ . (The two bands seen in Fig. 1b arise due to the up/down channel configuration of our experiment, see Supplementary Information (SI) for derivation details). The non-unitary time evolution of the walk leads to a nontrivial winding of  $\epsilon(k_x, k_y)$  for each band in the complex energy plane as one continuously varies Bloch vector  $(k_x, k_y)$

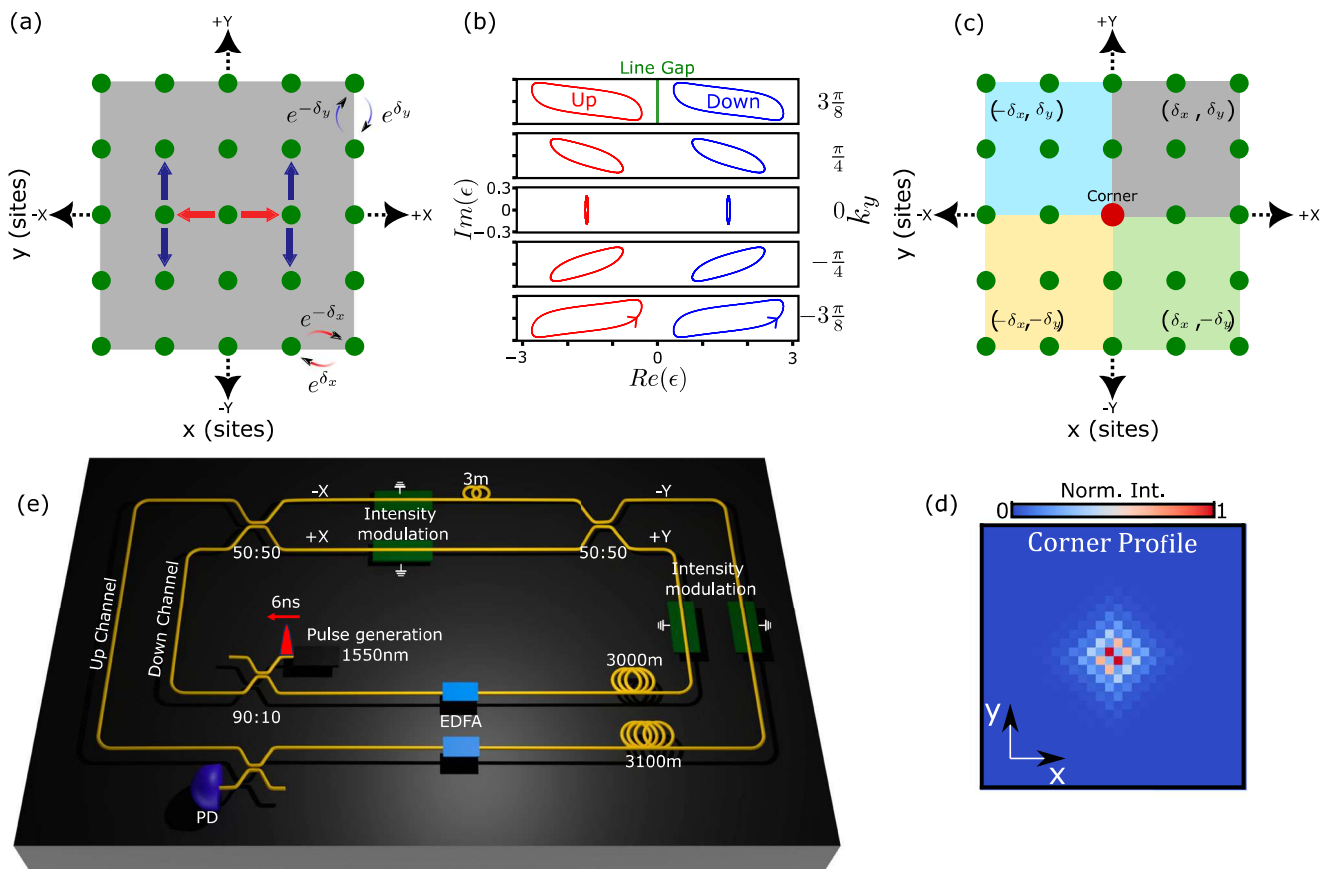


**Fig. 1 | Two-dimensional quantum walk in non-Hermitian synthetic lattice.** **a** Example of photonic quantum walk in a 2D synthetic lattice. The blue and red curved arrows show the direction-dependent loss and gain. **b** Winding of effective eigenenergies  $\epsilon_{up/down}(k_x, k_y)$  in the complex energy plane for a single bulk non-Hermitian lattice with periodic boundary condition, showing line-gapped topology (indicated by the green line). Here we choose five different values  $k_y \equiv 0, \pm \pi/4, \pm 3\pi/8$ . **c** Four bulk lattices with different gain-loss patterns are glued along their edges

to form a corner. Note that  $\delta_x > 0$  implies gain for a step towards  $-X$  and loss for a step toward  $+X$ . For  $\delta_x < 0$  the gain-loss is inverted. A similar rule applies for  $\delta_y$ . **d** Averaged spatial profile of corner skin modes formed in the system shown in **c**, by taking non-Hermitian parameters  $\delta_x = \delta_y = 0.175$ . The lattice size is  $30 \times 30$ . **e** The time-multiplexed experimental scheme, with which the lattice parameters can be (dynamically) controlled by the intensity modulators. EDFA: Erbium-doped fiber amplifier. PD: Photodiode.

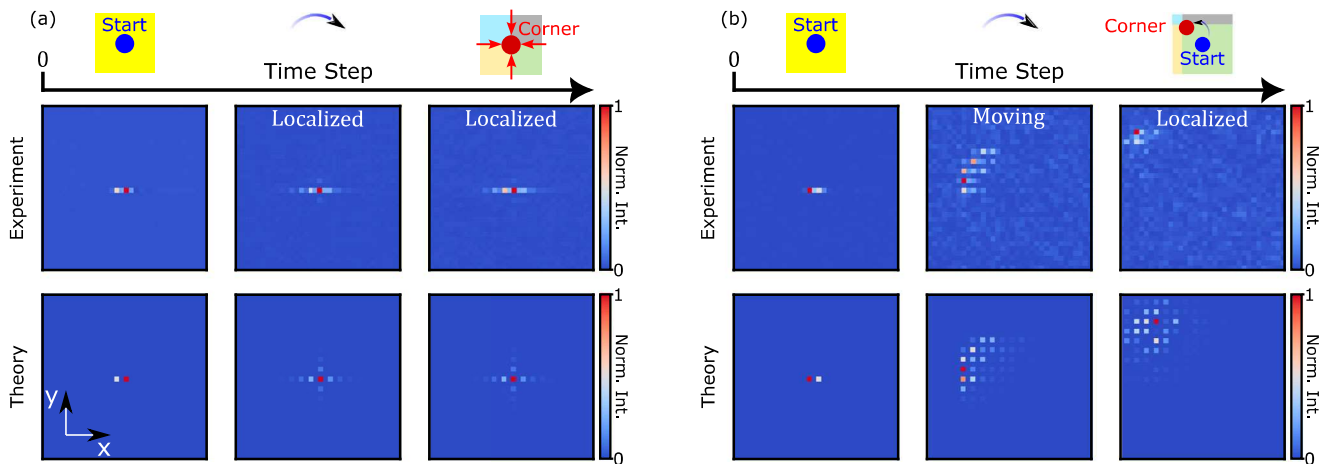


**Fig. 2 | Light localization and light funneling for static control. a** Light localization at the corner skin modes located at  $(x, y) = (0, 0)$  for non-Hermitian parameter  $|\delta_x| = |\delta_y| = 0.175$ . Here a single pulse is initialized at  $(x, y) = (0, 0)$  in the up channel. **b** Light funneling for the same lattice parameter and pulse initialization,

but the corner skin mode is located at  $(x, y) = (-10, 10)$ . Here the skin effect allows light to flow to the corner skin mode and localize there. In both **a** and **b**, from left to right the snapshots are shown for time steps 1, 9, 21, respectively.

along a certain curve in the Brillouin zone. To illustrate this, in Fig. 1b, we plot the complex energies  $\epsilon_{up/down}(k_x, k_y)$  of the bulk lattice shown in Fig. 1a as we vary  $k_x$  from  $-\pi$  to  $\pi$  while keeping  $k_y$  fixed to different values  $0, \pm\pi/4, \pm 3\pi/8$ . As  $(k_x, k_y)$  varies along each of these directed horizontal curves in the Brillouin zone, both  $\epsilon_{up}(k_x, k_y)$  and  $\epsilon_{down}(k_x, k_y)$  winds one loop in the counterclockwise direction, thus exhibiting an integer-valued winding number  $-1$ . This is a topological invariant for our non-Hermitian quantum walk. Also, the two winding loops contributed from the two bands  $\epsilon_{up/down}$  exhibit a line-gapped topology<sup>24</sup>, such that the two winding loops never cross the line  $Re(\epsilon) = 0$  in the complex plane. Windings of complex energy along other curves in the Brillouin zone are shown in the supplementary information (SI) section 3.

In a finite system, the nontrivial winding of the complex energies and the associated 2D non-Hermitian skin effect<sup>24</sup> is manifested as corner skin modes, that is, localization of the walker can happen at an interface between regions with opposite windings (or bulk band topologies). Figure 1c shows one exemplary case which consists of four distinct regions, represented by the four different color patches. The gray patch is identical to the system described in Fig. 1a. The other three regions exhibit an inverted gain-loss relation (indicated by a change in the sign of the gain parameter) either along the  $x$  or  $y$ -axis, or both. This inversion of gain-loss leads to different windings for each region. Non-Hermitian skin effect occurs in such a system, and we numerically verify in Fig. 1d that the averaged eigenmodes of the quantum walk exhibit clustering at the junction between the four regions - as indicated by the red dot in Fig. 1c.

To simulate the quantum walk described above, we use classical light pulses in a time-multiplexed setup shown in Fig. 1e. We note that for this linear system, the evolution of classical light pulses in the lattice exactly follows that of the quantum walk of single photons in the lattice. We map the state space of the 2D square lattice of size  $30 \times 30$  into different time-delays in two fiber feedback loops, as introduced in previous works<sup>25,26</sup>. To introduce non-Hermiticity, we use four intensity modulators that introduce individually controllable loss when the walker moves along any direction. We also use two erbium-doped fiber amplifiers (EDFAs) that provide gain in the system, and together with the intensity modulators, introduce a gain-loss mechanism that can be controlled at each step of the walker. We specifically choose electro-optic modulators with a high bandwidth to allow reconfigurability of the system's topology at each step of the quantum walk. A full discussion of the experimental setup is provided in the SI sections 1 and 2.

## Results

### Skin effect under static control

To show the presence of non-Hermitian corner skin modes, we first construct the model as shown in Fig. 1c, with the corner located at the lattice origin  $(x = 0, y = 0)$ . We inject a single light pulse into the time bin corresponding to the lattice origin and choose non-Hermitian parameters  $|\delta_x|$  and  $|\delta_y|$  to be 0.175 as in Fig. 1c. In Fig. 2a, we plot the snapshots of the light distribution in the lattice for different time steps 1, 9, and 21, which are obtained by measuring the pulse power at each time bin. The evolution of distribution shows that the walker stays localized at the origin, confirming the presence of a corner skin mode. In sharp contrast, when we set  $\delta_x$  and  $\delta_y$  to 0, we observe a significant spreading of the intensity distribution, indicating the absence of any corner skin modes (see Supplementary Sections 4 and 5 in the SI for the experimental data).

Having shown the localization of light at the corner skin mode, we next demonstrate the skin-effect-induced funneling of light. Namely, the system dynamics bring any initial state towards the corner skin modes. We set the corner skin mode to be at the lattice site  $(x = -10, y = 10)$  while light pulses are still injected at  $x = 0, y = 0$ , which is now in the bulk of the lattice (Fig. 2b). As the system evolves, initially light spreads in bulk, but finally converges to the corner site. As shown in the SI for several different lattice configurations, light pulses always converge to the corner regardless of the initialization location. This funneling of light to the corner skin mode is a manifestation of the skin effect where all the eigenmodes of the system are localized at the corner. Schematic illustration of this funneling effect can be seen in Supplementary Movie 1. Our experimental results are in good agreement with our theoretical prediction shown in Fig. 2b.

### Dynamically controlling the non-Hermitian lattice and skin effect

The use of time as a synthetic dimension allows us to dynamically reconfigure our non-Hermitian lattice as a function of time. Specifically, by controlling the intensity modulators at each time step of the quantum walk, we achieve temporal modulation of the gain/loss parameters  $\delta_x(t)$  and  $\delta_y(t)$  such that they are time-dependent. Using this time dependence, first, we demonstrate dynamical control over the degree of localization of the corner skin modes. At the start of the evolution, we adopt the configuration as in Fig. 1c and set  $|\delta_x(0)| = |\delta_y(0)| = 0.175$ , and inject a single light pulse at the corner skin mode situated at the origin. As the system evolves, we reduce both  $|\delta_x|, |\delta_y|$  by 50% for every four time-steps and continue doing so until step 16

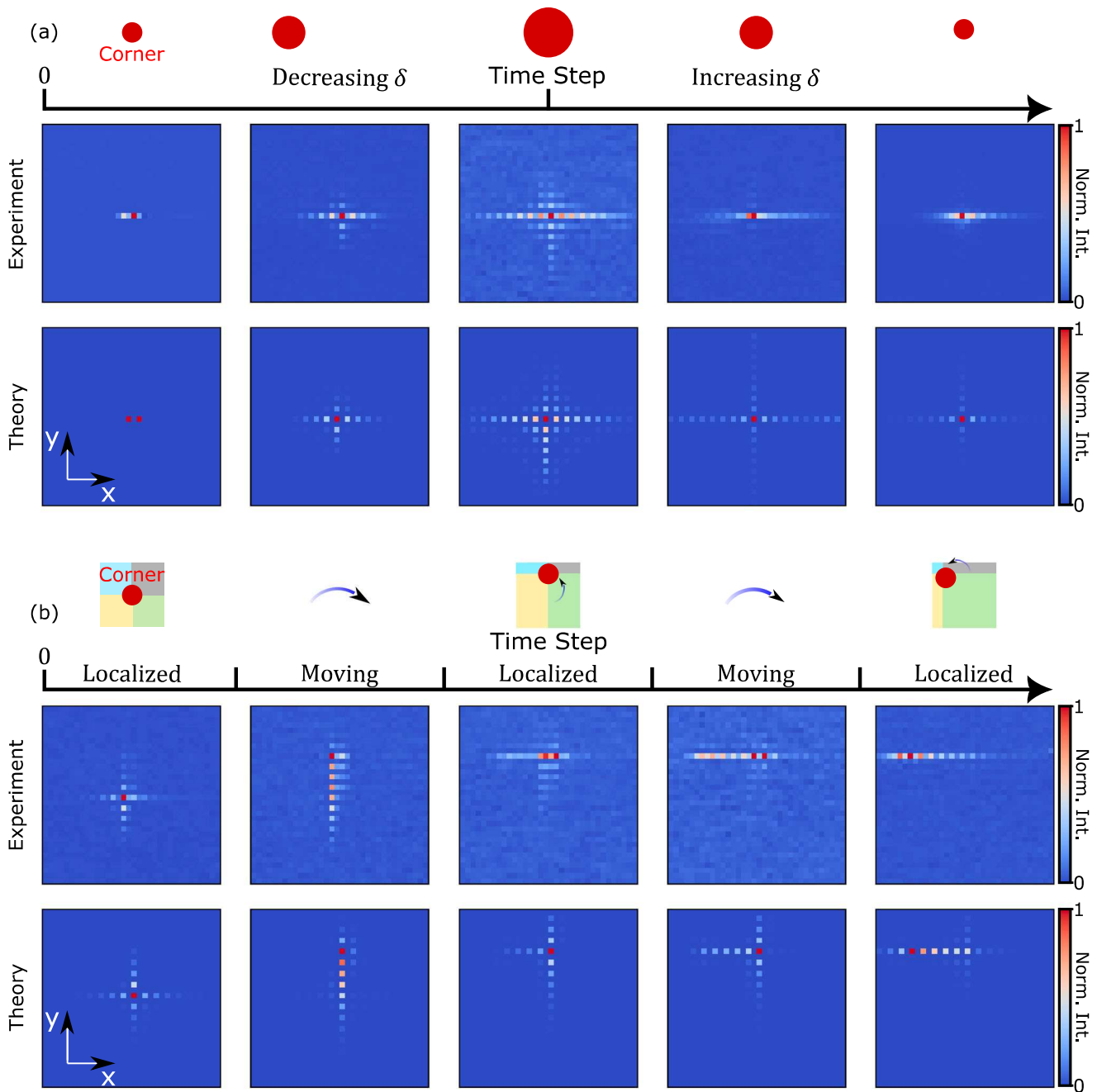


**Fig. 3 | Dynamical control of the corner skin mode.** **a** Dynamical control of corner skin mode spatial profile. As the non-Hermitian parameter is gradually reduced from  $|\delta_{x,max}| = |\delta_{y,max}| = 0.175$  to  $|\delta_{x,max}| = |\delta_{y,max}| = 0.02$  and back to  $|\delta_{x,max}| = |\delta_{y,max}| = 0.175$ , the corner skin mode becomes delocalized and then localized. From

left to right the snapshots are shown for time steps 1, 9, 17, 25, 37, respectively. **b** Dynamically tweezing localized light along a designed “L”-shaped trajectory using the skin effect. Localized light is first moved in the +Y direction for 8 steps and then to the -X direction for 10 steps.

(Fig. 3a). Because of this reduction, we observe that the corner skin modes become less confined to the origin. This is because the smaller non-Hermitian parameter exhibits eigenmodes distributed over a larger area, as predicted theoretically (see Supplementary Fig. S4 in the SI). Thereafter, starting from step 17, we reverse the process, that is, we increase the gain/loss parameters  $|\delta_x|, |\delta_y|$  back to its original value at the same rate. We now observe a relocalization of light at the origin.

Next, we demonstrate gradual repositioning of the corner skin modes in the lattice. We use the same lattice geometry shown in Fig. 1c and fix the non-Hermitian parameter to  $\delta_x = \delta_y = 0.175$ . As the system evolves, we gradually move the interface between the four distinct topological regions, repositioning the corner skin mode as a function of time. We first move the position of the corner skin mode upwards

for 8 unit cells, and then leftward for 10 unit cells. As before, we inject light pulses at the corner skin mode. As the system evolves, we observe that the center of the intensity distribution follows the position of the corner skin mode as it gradually moves along the given L-shaped trajectory from its initial location ( $x=0, y=0$ ) to its final location at ( $x=-10, y=8$ ). Furthermore, during this process, the intensity distribution remains tightly localized close to the corner skin mode. Evidently, the corner serves as a non-Hermitian tweezer of light, which allows us to gradually move trapped photons along a given trajectory in the synthetic lattice. Note that non-Hermitian light steering has been demonstrated in real-space lattices<sup>1</sup>, and our demonstration in synthetic time dimensions portends the potential for such photonic control using the temporal degree of freedom of light.



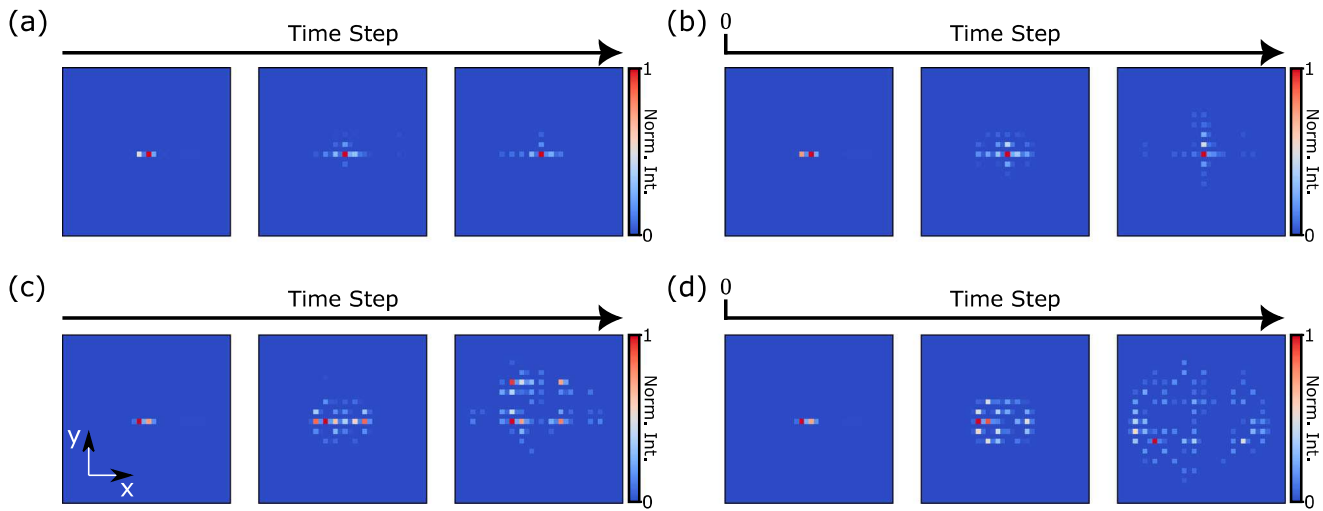


**Fig. 4 | Robustness of the skin effect at the presence of different degrees of lattice disorder.** The randomness is introduced to the intensity modulation of the lattice and the pulse is injected at  $(x, y) = (0, 0)$ . **a, b** Experimental observation of robustness of the corner skin mode and skin effect in a lattice with moderate disorder ( $\eta_y = \eta_x = 0.5, 1$ ). Here the disorder leads to a relaxed spatial confinement of

light without breaking the localization of light. **c, d** Breakdown of the localization in the presence of strong disorder ( $\eta_y = \eta_x = 1.5, 2$ ). Light can diffuse arbitrarily far away until they are limited by the size of the experiment. In **a–d**, from left to right the snapshots are shown for time steps 1, 5, 13, respectively.

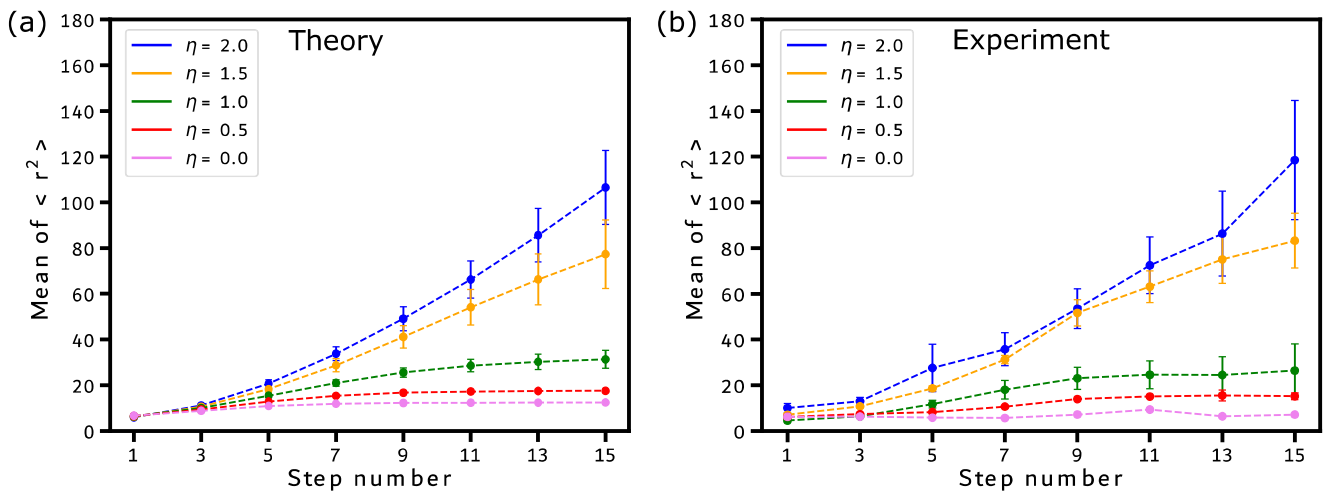


**Fig. 5 | Breakdown threshold of the robustness.** **a** Theory and **b** Experimental evolution of space-averaged displacement  $\langle r^2 \rangle = \langle x^2 + y^2 \rangle$  as a function of step number under different lattice disorders. For disorder strength lower than the threshold  $\eta = 1$ , the disorder increases the effective spatial diameter of the corner

skin mode, as shown in the evolution of average displacement with time. For disorders higher than the threshold, light diffusively spreads to large distances on the lattice. Standard deviations are also shown at each step.

Schematic illustrations of the tapering and relocation effects can be seen in Supplementary Movies 2 and 3, respectively.

### Robustness of the skin effect

The topological nature of the non-Hermitian skin effect ensures its robustness against disorder in gain/loss parameters  $\delta_x, \delta_y$ . To quantitatively investigate this robustness, we introduce a disorder on the gain/loss. At each lattice site, we randomly pick both  $\delta_x, \delta_y$  from a uniform distribution on the interval  $[\delta_{max}(1 - \eta), \delta_{max}]$ , where  $\delta_{max}$  is the maximum gain parameter and  $\eta$  is the disorder parameter which quantifies the variance of the gain parameter. In our experiment, we vary the disorder parameter between 0 (no disorder) and 2 (max disorder).

We find that the skin effect is robust when the disorder parameter  $\eta < 1$ . In Fig. 4a, b, we plot the evolution of light pulses in the lattice for two different values  $\eta = 0.5$  and  $\eta = 1$ . For both cases, we inject light pulses at the corner skin mode located at the origin. We observe that, even though the localization of the intensity distribution reduces as the disorder

increases, the distribution still stays confined around the origin, indicating the existence of corner skin modes even in the presence of disorder. Nevertheless, once we increase the disorder parameter to 1.5 and 2 (Fig. 4c, d), the intensity distribution diffusively spreads away from the origin, indicating the breakdown of corner skin mode. Our experimental observation agrees with the intuitively expected behavior that, for  $\eta < 1$ , even though there is a disorder in the modulation amplitudes, the gain for the step towards the corner is always larger than that of the outwards direction. Thus the four regions maintain their distinct non-Hermiticity and the corner skin mode exists. But, when  $\eta > 1$ , a direction-dependent gain for the time steps is no longer always valid and therefore the four regions are no longer distinct and the corner skin mode ceases to exist.

To better characterize the robustness and breakdown of the skin effect, we compute the evolution of the mean-square displacement of the intensity distribution in the lattice as a function of time. The mean-square displacement is quantified as  $\langle r^2 \rangle (n) = \sum_{x,y} P_{x,y}(n)(x^2 + y^2)$ , where  $P_{x,y}(n)$  is the time-varying intensity distribution of light. Figure 5

shows the calculated  $\langle r^2 \rangle (n)$  for several values of the disorder parameter for both theoretical calculations and experimentally measured values. Each experimental curve corresponds to an average of eight independent experimental realizations of disorder, while the theory corresponds to eight averages. Due to the limited size of the lattice ( $30 \times 30$ ), we only collect data from step 1 to step 15, and plot  $\langle r^2 \rangle (n)$  for the odd steps. The violet, red, and green curves correspond to the weak disorder, with disorder parameters being 0, 0.5, and 1, respectively. All three curves saturate to a fixed value which is well below a certain threshold. This behavior thus implies the robustness of the skin effect. However, for larger disorders of 1.5 and 2, corresponding to the yellow and blue curve, the mean squared distance does not converge. Instead, it spreads out until it becomes limited by the finite size of the lattice, indicating a complete breakdown of the skin effect.

## Discussion

In conclusion, we demonstrated robust dynamical control over the photonic non-Hermitian skin effect in a 2D synthetic lattice. We created a corner skin mode that localizes light and dynamically tuned the degree of light localization. Moreover, we dynamically steered trapped light along any given trajectory in the 2D lattice. We also demonstrate the robustness of the skin effect under lattice disorder below a certain threshold. Our results demonstrate that useful control mechanisms in spatial landscapes such as reconfigurable light steering<sup>1</sup> can be extended to synthetic dimensions.

Looking forward, the dynamic techniques developed in this work can be further applied to investigate Floquet non-Hermitian models<sup>27–29</sup>, in particular in synthetic dimensions<sup>30</sup>. Further, one can create an analogue of on-site interaction by imposing a nonlinear phase shifter after the linear optical transformations, and investigate non-Hermitian models of interacting particles<sup>31</sup>. Such nonlinearities could also have implications in the recently discovered regime of topological frequency combs<sup>32–34</sup> as well as temporal mode-locked lasers<sup>35</sup> due to the periodic temporal pulses that define our platform. Moreover, the two-fold spin characteristics in our system can potentially be extended to non-Hermitian models for lattice gauge theories with higher spins and non-Abelian statistics, by increasing the number of loops<sup>36</sup>. Another intriguing direction can be exploring NHSE-enabled morphing of photonic topological modes which was recently demonstrated in mechanical lattices<sup>37</sup>. Finally, our non-hermitian lattice can be enriched with engineered synthetic gauge fields<sup>38</sup> as demonstrated recently for both Hermitian<sup>39</sup> and non-Hermitian models<sup>20</sup>, to explore intriguing proposals such as the quantum Skin Hall effect<sup>40</sup>.

## Methods

### Experimental setup

To encode the 2D lattice in time we consider two fiber loops shown in Fig. 1, labeled up channel and down channel. The length of each fiber loop is  $\sim 3$  (km), and one circulation of light in the loop is equivalent to one step of the walk. Hence, we can encode the entire 2D lattice within a time-duration (or time-delay) of  $\sim 15,000$  (ns) without mixing time-bins in step  $n$  and step  $(n+1)$ . We first encode 30 Y-time bins in both the up and down channels, each of time duration 250 (ns) in a total time duration of 7500 (ns). Each Y-time bin is then occupied by 30 X-time bins, each of time duration 7.5 (ns). At any time, the state of the system is thus represented by a complex vector  $(U_{x,y}, D_{x,y})$ , encoded in the phase and amplitude of the light pulse circulating in the two fiber loops.

### Measurement

To initialize the system, we inject a single pulse into the down channel of the fiber loop. We use a continuous wave CW laser with 1550 (nm) wavelength (Optilab DFB-1551-SM-10) and by modulation of this laser using a Thorlabs SOA (SOA1013SXS), we have generated pulses of width  $\sim 6$  (ns) at a repetition rate of 1 (pulse/ms). We then control the

polarization of the laser with an inline fiber polarization control (PC) before injecting the light into the down channel with a 90/10 beam splitter. Note that we use two identical 90/10 beam splitters, one for each channel. The 90/10 beam splitter in the down channel is used to inject light into the quantum walk, whereas the 90/10 beam splitter in the up channel is used to weakly couple light pulses out of the quantum walk so that we can measure the pulse power after  $n$  steps of evolution using the up channel's PD. Note that the EDFA placed immediately prior to the up channel's PD is merely used to amplify the light pulses coming out of the quantum walk experiment, making it easier for the PD to detect it.

As a pulse enters the system, by default we recognize it as entering the  $(x=0, y=0)$  time bin, and thus the initial state is  $D_{0,0}=1$ . The pulse then sequentially passes through a 50/50 beam splitter denoted as  $\pm X$ -beam splitter, a pair of time-varying intensity modulators (Optilab IMP-1550-20-PM) is used to impose the correct gain/loss as each time bin  $(x, y)$  passes through it, controlled by RF signal generated from Teledyne Lecroy arbitrary waveform generator (T3AWG3252). We then impose a delay of 3 (m) in the up channel and no delay in the down channel. The same procedure then repeats for  $Y$ .

To combat photon loss in the walk, we use two Thorlabs erbium-doped fiber amplifiers (EDFA) (EDFA100S), one for each channel. Before amplifying the pulse, we use wavelength division multiplexers (WDM) (DWDM-SM-1-34-L-1-2) to couple a 1543 (nm) CW laser (DFB-1543-SM-30) to the pulses so that the spontaneous emission noise during the amplification is reduced. We decouple the 1550 (nm) pulses from the 1543 (nm) CW laser with the same WDM after the amplification is done. Finally, we use PC to ensure the correct linear polarization for the 1550 (nm) signal pulses. After this, a complete quantum walk step is finished.

## Data availability

The data used in this study have been deposited in the Zenodo database under <https://doi.org/10.5281/zenodo.14207240>.

## Code availability

The codes used for the simulations presented in this study have been deposited in the Zenodo database under <https://doi.org/10.5281/zenodo.14207240>.

## References

- Chalabi, H. et al. Synthetic gauge field for two-dimensional time-multiplexed quantum random walks. *Phys. Rev. Lett.* **123**, 150503 (2019).
- Chalabi, H. et al. Guiding and confining of light in a two-dimensional synthetic space using electric fields. *Optica* **7**, 506–513 (2020).
- Chen, W., Kaya Özdemir, Ş., Zhao, G., Wiersig, J. & Yang, L. Exceptional points enhance sensing in an optical microcavity. *Nature* **548**, 192–196 (2017).
- Feng, L. et al. Experimental demonstration of a unidirectional reflectionless parity-time metamaterial at optical frequencies. *Nat. Mater.* **12**, 108–113 (2013).
- Flower, C. J. et al. Observation of topological frequency combs. *Science* **384**, 1356–1361 (2024).
- Gliozzi, J., De Tomasi, G. & Hughes, T. L. Many-body non-hermitian skin effect for multipoles. *arXiv* **2401**, 04162 (2024).
- Gong, Z. et al. Topological phases of non-hermitian systems. *Phys. Rev. X* **8**, 031079 (2018).
- Mehrabad, M. J. & Hafezi, M. Strain-induced Landau levels in photonic crystals. *Nat. Photonics* **18**, 527–528 (2024).
- Mehrabad, M. J., Mittal, S. & Hafezi, M. Topological photonics: Fundamental concepts, recent developments, and future directions. *Phys. Rev. A* **108**, 040101 (2023).
- Kawabata, K., Shiozaki, K. & Ueda, M. Anomalous helical edge states in a non-hermitian Chern insulator. *Phys. Rev. B* **98**, 165148 (2018).

11. Leefmans, C. R. et al. Topological temporally mode-locked laser. *Nat. Phys.* **20**, 1–7 (2024).
12. Liang, Q. et al. Dynamic signatures of non-hermitian skin effect and topology in ultracold atoms. *Phys. Rev. Lett.* **129**, 070401 (2022).
13. Lin, Q., Yi, W. & Xue, P. Manipulating directional flow in a two-dimensional photonic quantum walk under a synthetic magnetic field. *Nat. Commun.* **14**, 6283 (2023).
14. Lin, R., Tai, T., Li, L. & Lee, C. H. Topological non-hermitian skin effect. *Front. Phys.* **18**, 53605 (2023).
15. Lin, Z. et al. Observation of topological transition in floquet non-hermitian skin effects in silicon photonics. *Phys. Rev. Lett.* **133**, 073803 (2024).
16. Liu, Y. G. N. et al. Complex skin modes in non-hermitian coupled laser arrays. *Light.: Sci. Appl.* **11**, 336 (2022).
17. Yuhao, M. A. & Hughes, T. L. Quantum skin hall effect. *Phys. Rev. B* **108**, L100301 (2023).
18. Mittal, S., Moille, G., Srinivasan, K., Chembo, Y. K. & Hafezi, M. Topological frequency combs and nested temporal solitons. *Nat. Phys.* **17**, 1169–1176 (2021).
19. Nasari, H., Pyrialakos, G. G., Christodoulides, D. N. & Khajavikhan, M. Non-hermitian topological photonics. *Optical Mater. Express* **13**, 870–885 (2023).
20. Nitsche, T. et al. Quantum walks with dynamical control: graph engineering, initial state preparation and state transfer. *N. J. Phys.* **18**, 063017 (2016).
21. Okuma, N. & Sato, M. Non-hermitian topological phenomena: A review. *Annu. Rev. Condens. Matter Phys.* **14**, 83–107 (2023).
22. Okuma, N., Kawabata, K., Shiozaki, K. & Sato, M. Topological origin of non-hermitian skin effects. *Phys. Rev. Lett.* **124**, 086801 (2020).
23. Pang, Z., Wong, B. T. T., Hu, J. & Yang, Y. Synthetic non-abelian gauge fields for non-hermitian systems. *Phys. Rev. Lett.* **132**, 043804 (2024).
24. Schreiber, A. et al. A 2d quantum walk simulation of two-particle dynamics. *Science* **336**, 55–58 (2012).
25. Wang, K., Dutt, A., Wojcik, C. C. & Fan, S. Topological complex-energy braiding of non-hermitian bands. *Nature* **598**, 59–64 (2021).
26. Wang, K. et al. Generating arbitrary topological windings of a non-hermitian band. *Science* **371**, 1240–1245 (2021).
27. Wang, K., Xiao, L., Budich, J. C., Yi, W. & Xue, P. Simulating exceptional non-hermitian metals with single-photon interferometry. *Phys. Rev. Lett.* **127**, 026404 (2021).
28. Wang, W., Wang, X. & Ma, G. Non-hermitian morphing of topological modes. *Nature* **608**, 50–55 (2022).
29. Weidemann, S. et al. Topological funneling of light. *Science* **368**, 311–314 (2020).
30. Weidemann, S., Kremer, M., Longhi, S. & Szameit, A. Topological triple phase transition in non-hermitian floquet quasicrystals. *Nature* **601**, 354–359 (2022).
31. Wiersig, J. Review of exceptional point-based sensors. *Photonics Res.* **8**, 1457–1467 (2020).
32. Xiao, L. et al. Observation of non-bloch parity-time symmetry and exceptional points. *Phys. Rev. Lett.* **126**, 230402 (2021).
33. Yao, S. & Wang, Z. Edge states and topological invariants of non-hermitian systems. *Physical Rev. Lett.* **121**, 086803 (2018).
34. Yokomizo, K. & Murakami, S. Non-bloch band theory of non-hermitian systems. *Phys. Rev. Lett.* **123**, 066404 (2019).
35. Yuan, L., Lin, Q., Xiao, M. & Fan, S. Synthetic dimension in photonics. *Optica* **5**, 1396–1405 (2018).
36. Zhang, X., Zhang, T., Lu, M.-H. & Chen, Y.-F. A review on non-hermitian skin effect. *Adv. Phys. X* **7**, 2109431 (2022).
37. Zhao, H. et al. Non-hermitian topological light steering. *Science* **365**, 1163–1166 (2019).
38. Zhou, L. & Zhang, D.-J. Non-hermitian floquet topological matter—a review. *arXiv* **2305**, 16153 (2023).
39. Zhou, Q. et al. Observation of exceptional points and skin effect correspondence in non-hermitian phononic crystals. *Nat. Commun.* **14**, 4569 (2023).
40. Zou, D. et al. Observation of hybrid higher-order skin-topological effect in non-hermitian topoelectrical circuits. *Nat. Commun.* **12**, 7201 (2021).

## Acknowledgements

The authors wish to acknowledge fruitful discussions with Shanhui Fan and Nathan Schine. This research was supported by The Office of Naval Research ONR-MURI grant N00014–20–1–2325, AFOSR FA95502010223, NSF OMA1936314, NSF PHY1820938, IMOD NSF DMR –2019444 and the Army Research Laboratory grant W911NF1920181.

## Author contributions

X.Z. and M.J.M. performed the experiments and theory and analyzed the data. X.Z., M.J.M. and S.M. constructed the experimental setup with help from J.V. and K.L. E.W., S.M., M.H., and A.D. supervised the project and interpretation of the data. E.W., M.J.M., and X.Z. wrote the manuscript with input from all authors.

## Competing interests

The authors declare no competing interests.

## Additional information

**Supplementary information** The online version contains supplementary material available at <https://doi.org/10.1038/s41467-024-55236-4>.

**Correspondence** and requests for materials should be addressed to Mahmoud Jalali Mehrabad, Sunil Mittal or Edo Waks.

**Peer review information** *Nature Communications* thanks Baile Zhang, Alexander Khanikaev and the other, anonymous, reviewer(s) for their contribution to the peer review of this work. A peer review file is available.

**Reprints and permissions information** is available at <http://www.nature.com/reprints>

**Publisher's note** Springer Nature remains neutral with regard to jurisdictional claims in published maps and institutional affiliations.

**Open Access** This article is licensed under a Creative Commons Attribution-NonCommercial-NoDerivatives 4.0 International License, which permits any non-commercial use, sharing, distribution and reproduction in any medium or format, as long as you give appropriate credit to the original author(s) and the source, provide a link to the Creative Commons licence, and indicate if you modified the licensed material. You do not have permission under this licence to share adapted material derived from this article or parts of it. The images or other third party material in this article are included in the article's Creative Commons licence, unless indicated otherwise in a credit line to the material. If material is not included in the article's Creative Commons licence and your intended use is not permitted by statutory regulation or exceeds the permitted use, you will need to obtain permission directly from the copyright holder. To view a copy of this licence, visit <http://creativecommons.org/licenses/by-nc-nd/4.0/>.

© The Author(s) 2024

## CONTENTS

Experimental Setup	i
Mathematical formulation of the quantum walk experiment	iii
Effective band and energy winding of the bulk model	v
Localized eigenmodes at the presence of boundary and corner	vi
Static control supplementary data	vii
References	viii

### Experimental Setup

Here we show the details of the experimental setup.

To encode the 2D lattice in time we consider two fiber loops shown in Figure S1(a), labeled up channel and down channel. The length of each fiber loop is  $\sim 3$  (km), and one circulation of light in the loop is equivalent to one step of the walk. Hence, we can encode the entire 2D lattice within a time-duration (or time-delay) of  $\sim 15000$  (ns) without mixing time-bins in step  $n$  and step  $(n + 1)$ . As in Figure S1(b), we first encode 30 “Y”-time bins in both the up and down channel, each of time duration 250 (ns) in a total time duration of 7500 (ns). Each “Y”-time bin is then occupied by 30 “X”-time bins, each of time duration 7.5 (ns). At any time, the state of the system is thus represented by a complex vector  $(U_{x,y}, D_{x,y})$ , encoded in the phase and amplitude of the light pulse circulating in the two fiber loops. We note that in our designed allocation configuration, in particular, the time delay durations, we have chosen shorter delays than in previous 2D synthetic works. This is because, unlike the previously mentioned works where AOMs were used for switching, we have used EOMs which are much faster and can accommodate shorter delays [1, 2].

To initialize the system, we inject a single pulse into the down channel of the fiber loop. We use a continuous wave CW laser with 1550 (nm) wavelength (Optilab DFB-1551-SM-10) and by modulation of this laser using a Thorlabs SOA (SOA1013SXS), we have generated pulses of width  $\sim 6$  (ns) at a repetition rate of 1 (pulse/ms). We then control the polarization of the laser with an inline fiber polarization control (PC) before injecting the light into the down channel with a 90/10 beam splitter. Note that we use two identical 90/10 beam splitters, one for each channel. The 90/10 beam splitter in the down channel is used to inject light into the quantum walk, whereas the 90/10 beam splitter in the up channel is used to weakly couple light pulses out of the quantum walk so that we can measure the pulse power after  $n$  steps of evolution using the up channel’s PD. Note that the EDFA placed immediately prior to the up channel’s PD is merely used to amplify the light pulses coming out of the quantum walk experiment, making it easier for the PD to detect it.

As a pulse enters the system, by default we recognize it as entering the  $(x = 0, y = 0)$  time bin, and thus the initial state is  $D_{0,0} = 1$ . The pulse then sequentially passes through a 50/50 beam splitter denoted as  $\pm X$ -beam splitter, a pair of time-varying intensity modulators (Optilab IMP-1550-20-PM) is used to impose the correct gain/loss as each time bin  $(x, y)$  passes through it, controlled by RF signal generated from Teledyne Lecroy arbitrary waveform generator (T3AWG3252). We then impose a delay of 3 (m) in the up channel and no delay in the down channel. The same procedure then repeats for  $Y$ , as shown in Figure S1(a), except the difference in delay between the up and down channels is 100 (m).



To combat photon loss in the walk, we use two Thorlabs erbium-doped fiber amplifiers (EDFA) (EDFA100S), one for each channel. Before amplifying the pulse, we use wavelength division multiplexers (WDM) (DWDM-SM-1-34-L-1-2) to couple a 1543 (nm) CW laser (DFB-1543-SM-30) to the pulses so that the spontaneous emission noise during the amplification is reduced. We decouple the 1550 (nm) pulses from the 1543 (nm) CW laser with the same WDM after the amplification is done. Finally, we use PC to ensure the correct linear polarization for the 1550 (nm) signal pulses. After this, a complete quantum walk step is finished.

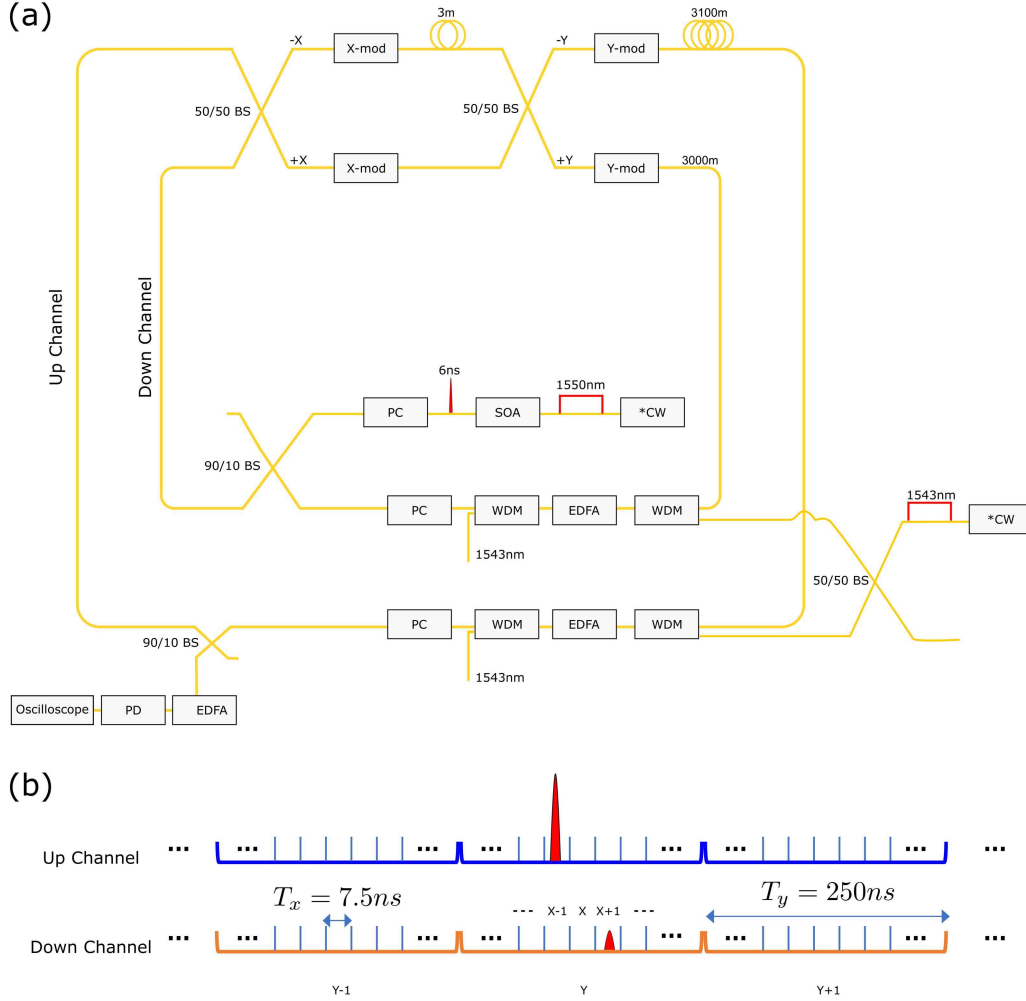


FIG. S1. **Sketch of the complete experimental setup and encoding scheme.** (a) Details of the experiment, with continuous wave (CW) laser, polarization control (PC), wavelength division multiplexer (WDM), photodiode (PD), beam splitter (BS), intensity modulators (X/Y-mod), erbium-doped fiber amplifier (EDFA) and semiconductor optical amplifier (SOA). (b) Encoding the 2D lattice in time bins in two fiber loops. The two loops are named “up channel” and “down channel”, respectively.

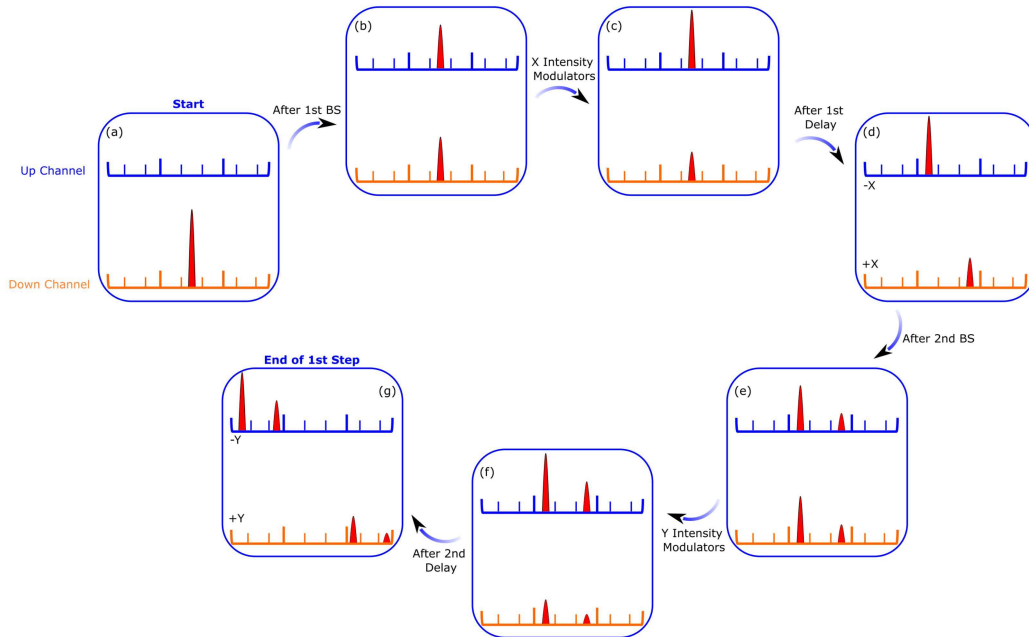


FIG. S2. **Example of full evolution in a complete step.** Both the up and down channels of the fiber loops are shown. (a-g) The complete evolution within one step given that the initial state is  $D_{x=0,y=0} = 1$  and all other  $U_{x,y}$  and  $D_{x,y}$  are 0.

### Mathematical formulation of the quantum walk experiment

Here we give the most general mathematical formulation of our quantum walk. Figure S2(a-g) shows this evolution when the input state is  $D_{0,0} = 1$ .

As mentioned in the previous section, the state at each step is given by a complex vector  $(U_{x,y}, D_{x,y})$  where  $x$  and  $y$  ranges from  $-15$  to  $+15$ . After the first beam splitter ( $\pm X$ ), the state is updated to (Figure S2(b)):

$$\begin{aligned} U'_{x,y} &= \frac{1}{\sqrt{2}}(U_{x,y} - D_{x,y}) \\ D'_{x,y} &= \frac{1}{\sqrt{2}}(U_{x,y} + D_{x,y}) \end{aligned} \quad (\text{S1})$$

After the first pair of modulators ( $\pm X$  modulators), we obtain:

$$\begin{aligned} U''_{x,y} &= U'_{x,y} f_{x,y}^{(U)} \\ D''_{x,y} &= D'_{x,y} f_{x,y}^{(D)} \end{aligned} \quad (\text{S2})$$

where  $f_{x,y}^{(U/D)}$  is the gain/loss applied to each time bin in the up/down channel by the  $X$  modulators.

After the delay:

$$\begin{aligned} U_{x,y}''' &= U_{x+1,y}'' \\ D_{x,y}''' &= D_{x-1,y}'' \end{aligned} \quad (\text{S3})$$

This yields:

$$\begin{aligned} U_{x,y}''' &= \frac{1}{\sqrt{2}}(U_{x+1,y} - D_{x+1,y})f_{x+1,y}^{(U)} \\ D_{x,y}''' &= \frac{1}{\sqrt{2}}(U_{x-1,y} + D_{x-1,y})f_{x-1,y}^{(D)} \end{aligned} \quad (\text{S4})$$

Then, we enter the second beamsplitter ( $\pm Y$ ):

$$\begin{aligned} W'_{x,y} &= \frac{1}{\sqrt{2}}(U_{x,y}''' - D_{x,y}''') \\ F'_{x,y} &= \frac{1}{\sqrt{2}}(U_{x,y}''' + D_{x,y}''') \end{aligned} \quad (\text{S5})$$

After modulation ( $\pm Y$  modulators):

$$\begin{aligned} W''_{x,y} &= W'_{x,y}c_{x,y}^{(U)} \\ F''_{x,y} &= F'_{x,y}c_{x,y}^{(D)} \end{aligned} \quad (\text{S6})$$

where  $c_{x,y}^{(U/D)}$  is the gain/loss applied to each time bin in the up/down channel by the  $Y$  modulators.

After delay:

$$\begin{aligned} W'''_{x,y} &= W''_{x,y+1} = \frac{1}{\sqrt{2}}(U_{x,y+1}''' - D_{x,y+1}''') \times c_{x,y+1}^{(U)} \\ F'''_{x,y} &= F''_{x,y-1} = \frac{1}{\sqrt{2}}(U_{x,y-1}''' + D_{x,y-1}''') \times c_{x,y-1}^{(D)} \end{aligned} \quad (\text{S7})$$

$(W'''_{x,y}, F'''_{x,y})$  is thus the output state given the input state  $(U_{x,y}, D_{x,y})$ . Consider a pulse ending up in time bin  $(x, y)$  at step  $(n+1)$ . Denoting it as  $U_{x,y}^{(n+1)}$  and  $D_{x,y}^{(n+1)}$ , we have:

$$\begin{aligned} U_{x,y}^{(n+1)} &= \frac{1}{2}[(U_{x+1,y+1}^{(n)} - D_{x+1,y+1}^{(n)})f_{x+1,y+1}^{(U)}c_{x+1,y+1}^{(U)} - (U_{x-1,y+1}^{(n)} + D_{x-1,y+1}^{(n)})f_{x-1,y+1}^{(D)}c_{x-1,y+1}^{(U)}] \\ D_{x,y}^{(n+1)} &= \frac{1}{2}[(U_{x+1,y-1}^{(n)} - D_{x+1,y-1}^{(n)})f_{x+1,y-1}^{(U)}c_{x+1,y-1}^{(D)} + (U_{x-1,y-1}^{(n)} + D_{x-1,y-1}^{(n)})f_{x-1,y-1}^{(D)}c_{x-1,y-1}^{(D)}] \end{aligned} \quad (\text{S8})$$

The above equation thus describes the full evolution of the state within one step. We can obtain lattice gain/loss pattern as shown in Figure 1(a) or in Figure 1(c) of the main text, by properly choosing  $f^{(U/D)}$  and  $c^{(U/D)}$  as a function of  $(x, y)$ . For example, for a bulk lattice as shown in Figure 1(a) of the main text, we choose  $f_{x,y}^{(U)} = \alpha e^{0.175}$ ,  $f_{x,y}^{(D)} = \alpha e^{-0.175}$ ,  $c_{x,y}^{(U)} = \alpha e^{0.175}$ ,  $c_{x,y}^{(D)} = \alpha e^{-0.175}$ . Here  $\alpha$  is the additional loss imposed by the modulators, and we use EDFA to compensate for the loss such that effectively,  $\alpha = 1$ . In the experiment, we are only measuring light in the up channel, and thus the power of pulses, or the probability distribution of the walker in the up channel, is

$P_{x,y} \propto |U_{x,y}|^2$ . We normalize this probability distribution for all experiment data. Importantly, we also note that while the signal-to-noise ratio is always decreasing as a function of the time step as seen in all the static control measurements, the power intensity distribution in the lattice also changes as a function of the degree of localization of light. This is particularly important in dynamic control over the localization of light at the corner as well as tweezing measurements when the light is localized at the corner after spreading.

### Effective band and energy winding of the bulk model

Here we impose periodic boundary conditions for the bulk lattice as shown in Figure 1(a) of the main text, in both  $X$  and  $Y$  directions. The modulations are  $f_{x,y}^{(U)} = e^{0.175}$ ,  $f_{x,y}^{(D)} = e^{-0.175}$ ,  $c_{x,y}^{(U)} = e^{0.175}$ ,  $c_{x,y}^{(D)} = e^{-0.175}$ , and thus  $\delta_x = 0.175$  and  $\delta_y = 0.175$ . With this assumption, we can therefore apply the Bloch theorem to the quantum walk evolution equation in the previous section and introduce the Bloch vector  $(k_x, k_y)$ . We use the ansatz  $U_{x,y} = e^{ik_x x + ik_y y} \tilde{U}_{k_x, k_y}$  and  $D_{x,y} = e^{ik_x x + ik_y y} \tilde{D}_{k_x, k_y}$  for the eigenmodes of the walk. The evolution equation can now be simplified to:

$$\begin{bmatrix} \tilde{U}_{k_x, k_y} \\ \tilde{D}_{k_x, k_y} \end{bmatrix} = \frac{1}{2} \begin{bmatrix} e^{ik_x + ik_y} f^{(U)} c^{(U)} - e^{-ik_x + ik_y} f^{(D)} c^{(U)} & -e^{ik_x + ik_y} f^{(U)} c^{(U)} - e^{-ik_x + ik_y} f^{(D)} c^{(U)} \\ e^{ik_x - ik_y} f^{(U)} c^{(D)} + e^{-ik_x - ik_y} f^{(D)} c^{(D)} & -e^{ik_x - ik_y} f^{(U)} c^{(D)} + e^{-ik_x - ik_y} f^{(D)} c^{(D)} \end{bmatrix} \begin{bmatrix} \tilde{U}_{k_x, k_y} \\ \tilde{D}_{k_x, k_y} \end{bmatrix} \quad (\text{S9})$$

Since we have two discrete degrees of freedom  $U$  and  $D$ , we always obtain two different eigenvalues for each  $(k_x, k_y)$  as we diagonalize the above  $2 \times 2$  matrix. We call the two eigenvalues  $u_{k_x, k_y}$  and  $d_{k_x, k_y}$ . The two effective energies are thus defined as  $\epsilon_{up}(k_x, k_y) = i \log(u_{k_x, k_y})$  and  $\epsilon_{down}(k_x, k_y) = i \log(d_{k_x, k_y})$ .

We further consider the four bulk patches in Figure S3(b) and show that they exhibit different non-Hermitian topological invariants, namely the winding of the effective energy  $\epsilon_{up/down}(k_x, k_y)$  in the complex plane. Without loss of generality, we always pick two loops in the Brillouin zone:  $l_v = \{k_x \equiv \pi/4, k_y \in [-\pi \rightarrow \pi]\}$  and  $l_h = \{k_y \equiv \pi/4, k_x \in [-\pi \rightarrow \pi]\}$ , as shown in Figure S3(a). For each bulk panel in Figure S3(b), as one varies  $(k_x, k_y)$  along  $l_v$  and  $l_h$ , the corresponding complex energy  $\epsilon(k_x, k_y)$  can finish a single loop in the complex plane, either in the clockwise or counterclockwise direction. The winding direction of  $\epsilon(l_v)$  and  $\epsilon(l_h)$  forms the non-Hermitian topological invariant of the bulk. Note that we have suppressed the unimportant label *up* and *down* since  $\epsilon_{up}(l_i)$  and  $\epsilon_{down}(l_i)$  always wind in the same direction. We note that the formation of corner skin modes in our semi-infinite system is guaranteed by the non-trivial winding in the complex energy plane. In particular, the four domains with different complex hoppings exhibit different directions of winding. At an interface between domains with different windings, we observe skin modes, as shown in Fig.1d in the main text. This phenomenon is similar to that of Hermitian topological systems where two regions with different winding numbers (or topological invariants) show edge modes.

A detailed discussion of the robustness of the corner skin modes is available in Ref. [3].



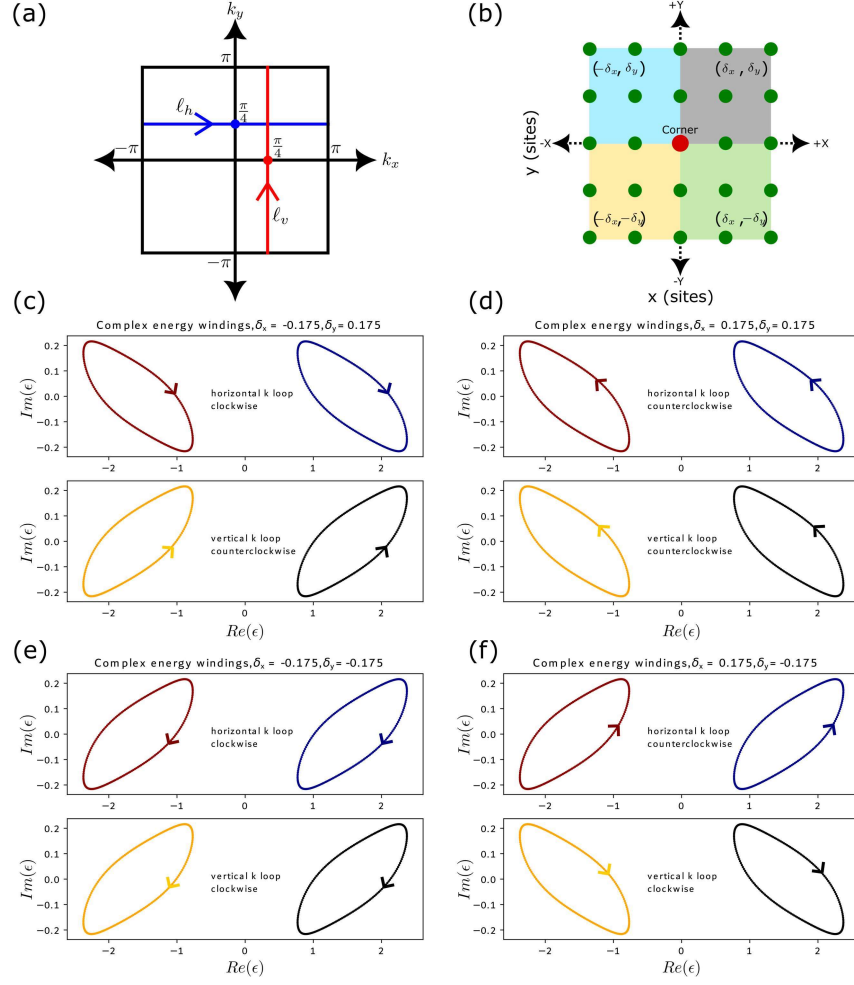


FIG. S3. **Bulk band non-Hermitian topology.** (a) For each bulk patch, we choose two oriented loops in the Brillouin zone:  $l_h = \{k_y \equiv \pi/4, k_x \in [-\pi \rightarrow \pi]\}$  and  $l_v = \{k_x \equiv \pi/4, k_y \in [-\pi \rightarrow \pi]\}$ . Each loop  $l_i$  then contributes to two individual complex energy winding loops  $\epsilon_{up}(l_i)$  and  $\epsilon_{down}(l_i)$  winding in the same direction. We calculate this winding for all four patches in (b), corresponding to positive or negative  $\delta_x$  and  $\delta_y$ . (c-f) The topological invariant is the winding direction of the directed curve  $\epsilon(l_h)$  and  $\epsilon(l_v)$  in the complex energy plane, which can either be clockwise or counterclockwise.

### Localized eigenmodes at the presence of boundary and corner

As shown in Figure 1(d) in the main text, the averaged spatial profile of the eigenmodes of the walk is localized at the corner. In Figure 1(c) of the main text we have chosen  $\delta_x = \delta_y = 0.175$ , but the feature of the spatial profile persists for any  $\delta_x = \delta_y > 0$ . Here in Figure S4 of the supplementary section, we show the average eigenmode spatial profile for  $\delta_x = \delta_y = 0.03, 0.06, 0.09, 0.12, 0.15$  and  $0.18$ . As one increases  $\delta_x = \delta_y$ , we observe that the averaged spatial profile becomes more localized.

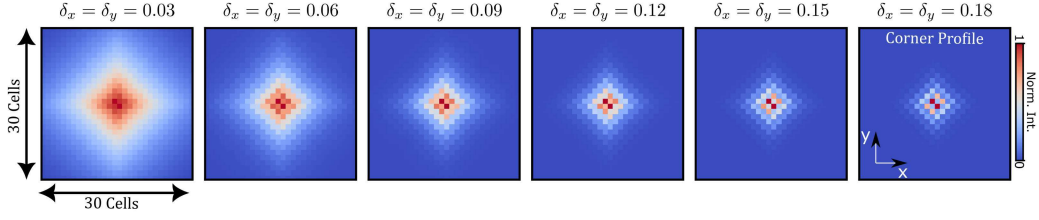


FIG. S4. **Averaged eigenmode spatial profile for different non-Hermitian parameters  $\delta_x = \delta_y$ .** We adopt the lattice geometry as in Figure S3(b). From left to right we take values 0.03, 0.06, 0.09, 0.12, 0.15 and 0.18.

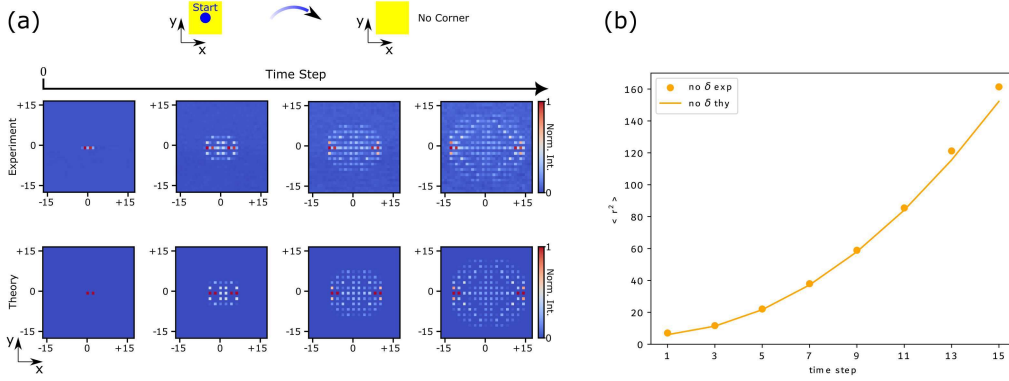


FIG. S5. **Evolution of probability distribution for non-Hermitian parameters  $\delta_x = \delta_y = 0$ , showing diffusive spreading.** (a) Probability distribution evolution, where the snapshots are taken at time step 1, 5, 9, 13, respectively. (b) Evolution of averaged displacement  $\langle r^2 \rangle = \langle x^2 + y^2 \rangle = \sum_{x,y} P_{x,y}(x^2 + y^2)$  for time step from 1, 3, 5, 7, 9, 11, 13 and 15.

This explains the gradual tapering of the walker's probability distribution as one increases/decreases the non-Hermitian parameter in time, as shown in Figure 3(a) in the main text.

### Static control supplementary data

Here we present additional experimental results for the quantum walk with no dynamical control. We first show that, with  $\delta_x = \delta_y = 0$ , the walker diffusively spreads into the bulk of the lattice, as shown in Figure S5(a), where the probability distribution of the walker is plotted for step 1, 5, 9, 13. The averaged displacement, defined as  $\langle r^2 \rangle (n) = \sum_{x,y} P_{x,y}(n)(x^2 + y^2)$ , is plotted in Figure S5(b), for step 1, 3, 5, 7, 9, 11, 13 and 15. Here  $P_{x,y}$  is the probability distribution of the walker at time step  $n$ .

Furthermore, as mentioned in the main text, the funneling of light happens wherever the walker is initialized, assuming the lattice gain-loss pattern shown in Figure 1(c) of the main text. This is manifestly shown in Figure S6, where we always choose the initial state to be  $D_{x=0,y=0} = 1$ , but lattice corner is located at  $(10, -10)$ ,  $(10, 10)$  and  $(-10, -10)$ , respectively.

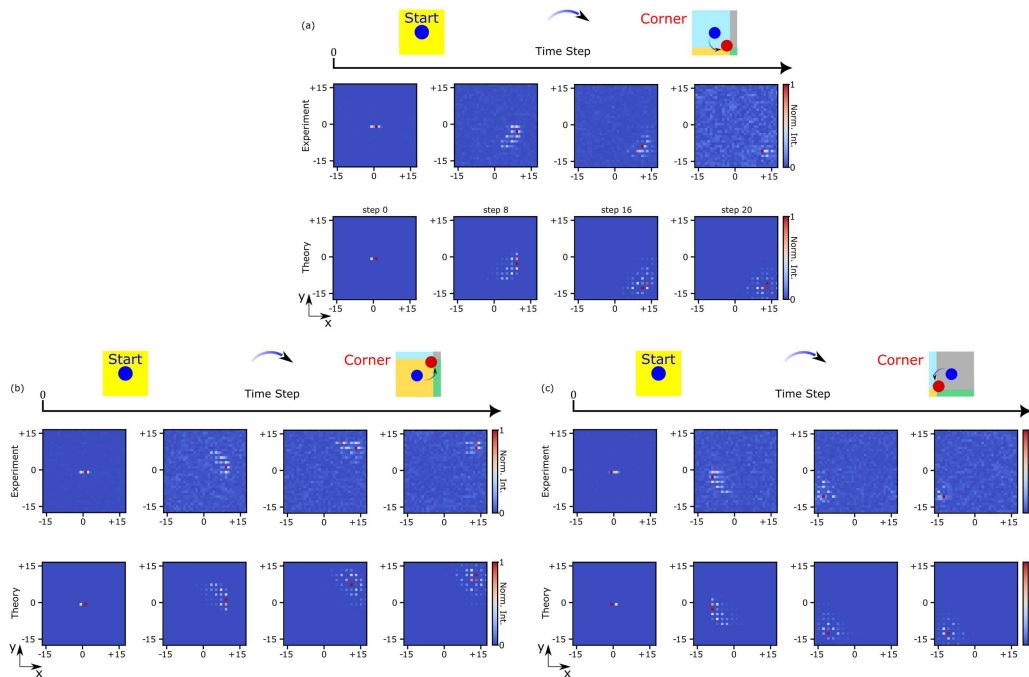


FIG. S6. **Funneling and stabilization of light starting from arbitrary bulk patches.** Light is always initialized at  $(x, y) = (0, 0)$ , but the corner position is held fixed at (a)  $(10, -10)$ , (b)  $(10, 10)$  and (c)  $(-10, -10)$ . For each panel, the top row is probability distributions collected at step 1, 9, 17, 21 of the experiment, and the bottom row is the corresponding simulation results.

- 
- [1] A. Schreiber, A. Gábris, P. P. Rohde, K. Laiho, M. Štefaňák, V. Potoček, C. Hamilton, I. Jex, and C. Silberhorn, *Science* **336**, 55 (2012).
  - [2] A. L. Muniz, M. Wimmer, A. Bisianov, U. Peschel, R. Morandotti, P. S. Jung, and D. N. Christodoulides, *Physical Review Letters* **123**, 253903 (2019).
  - [3] Z. Gong, Y. Ashida, K. Kawabata, K. Takasan, S. Higashikawa, and M. Ueda, *Physical Review X* **8**, 031079 (2018).